Supporting Information

p-n junction-induced bipolar charge micro-regions driving enhanced redox kinetics for efficient overall water splitting

Guangping Yang[a], Tianxiang Yang[a], Qing Pang[b], Menglong Sun[a], Xiaorong Xu[a], Zhiguo Wang[a], Abdullah Nasir[a], Sining Yun[a,*]

[a]*Functional Materials Laboratory (FML), School of Materials Science and Engineering, Xi'an University of Architecture and Technology, Xi'an, Shaanxi, 710055, China.*

[b]*College of Science, Xi'an University of Architecture and Technology, Xi'an, Shaanxi 710055, China*

* Corresponding author:

Sining Yun (alexsyun1974@aliyun.com; yunsining@xauat.edu.cn)

1. Electrochemical Measurements

Electrochemical tests employed a standard three-electrode system using a CHI 660E workstation. Catalyst-loaded nickel foam (NF), a graphite rod, and a Hg/HgO electrode served as the working (WE), counter (CE), and reference electrode. Linear sweep voltammetry (LSV) was performed at 5 mV s^{-1} with 95% iR compensation. Electrochemical impedance spectroscopy (EIS) was carried out from 0.1 to 100 kHz with a 5 mV AC amplitude. Mott-Schottky measurements used the same system with an Ag/AgCl reference in 0.5 M Na_2SO_4 at 1 kHz, scanning from -1 to 2 V vs. Ag/AgCl.

The overall water-splitting performance was evaluated on a two-electrode system by using NF loaded with electrocatalyst as cathode and anode in 1.0 M KOH.

2. COMSOL Multiphysics Simulations.

Finite element simulations were performed using COMSOL Multiphysics® v5.6. Two geometric models were constructed: (1) SCN@NiFe composites with randomly distributed NiFe LDH nanosheets (300-500 nm size, 30-60% surface coverage) on SCN nanotubes (10 μm length, 2 μm diameter), generated using built-in randomization algorithms; (2) Pure SCN nanotubes without nanosheet modification (control).

Coupled electric field and ion concentration distributions were solved via the steady-state Poisson-Nernst-Planck formalism, implemented through the electrostatics and transport of diluted species modules. The electrolyte domain (containing 1 M KOH and 0.5 M H_2SO_4) completely surrounds the catalytic structure, with diffusion coefficients for cations and anions set at 2.14×10^{9} m^2/s and 7×10^{9} m^2/s, respectively, and an electrolyte conductivity of 2.5 S/m.

The electrode-electrolyte interface was modeled using the Gouy-Chapman-Stern framework, comprising compact and diffuse layers. The compact layer contains adsorbed hydrated anions, while the diffuse layer accommodates a bulk electrolyte distribution. A constant electric field was assumed in the compact layer, whereas the diffuse layer field distribution satisfies the Poisson equation. Ion distributions across both layers were governed by the Poisson-Nernst-Planck Eq. (S1-S3).

$$\nabla \cdot (D_i \cdot \nabla c_i - z_i u_i F c_i \nabla V) = 0 \quad (S1)$$

$$\nabla^2 V = 0 (d < d_z) \quad (S2)$$

$$\nabla^2 V = -\frac{\rho}{\varepsilon_0 \varepsilon_r} (d < d_z) \quad (S3)$$

Where D_i represents the diffusion coefficients of OH^- and H^+ (5.23×10^{-5} cm^2/s and 1.35×10^{-5} cm^2/s, respectively), c_i represents the concentrations of OH^- and H^+, z_i represents the valences of all the ions, u_i represents the ionic migration ratios of different ions, F is the Faraday constant, V is the potential, and ρ is the charge density.

Electrode kinetics were modeled using the Butler-Volmer equation, where the anodic and cathodic charge transfer coefficients were set to 0.5 each, at T = 298.15 K, with exchange current density calculated via the Arrhenius relationship using material-specific activation energies.

3. Calculation Method for Turnover Frequency.

The intrinsic activity of the catalysts was evaluated by their turnover frequency (TOF), defined as the number of H_2 molecules evolved per second per active site.[1, 2] As expressed in Eq. (S4):

$$TOF = \frac{\#\ total\ hydrogen\ turnovers/cm^2 geometricareaarea}{\#\ active\ sites/cm^2 geometricareaarea} \ldots (S4)$$

The total hydrogen conversion (THC), required for the TOF calculation, was derived from the current density in the LSV polarization curve using Eq. (S5):

$$THF = \left(|j|\frac{mA}{cm^2}\right)\left(\frac{1C/S}{1000\ mA}\right)\left(\frac{1\ mol\ e^-}{96485\ C}\right)\left(\frac{1\ mol}{2\ mol\ e^-}\right)\left(\frac{N_A moleculars\ H_2}{1\ mol\ H_2}\right) \ldots (S5)$$

The number of active sites (NAS) was determined based on the loading mass of the catalyst on the nickel foam electrode and the molar content of Ni and Fe centers, according to Eq. (S6).

$$NAS = \left(\frac{catalyst\ loading\ area\ (g/cm^2)}{M_{metal\ atom}\ (g/mol)}\right)\left(\frac{6.022\ \times\ 10^{23}\ metal\ atom}{1mol\ metal\ atom}\right) (S6)$$

The TOF values were calculated by incorporating the THC and NAS following the above procedure.

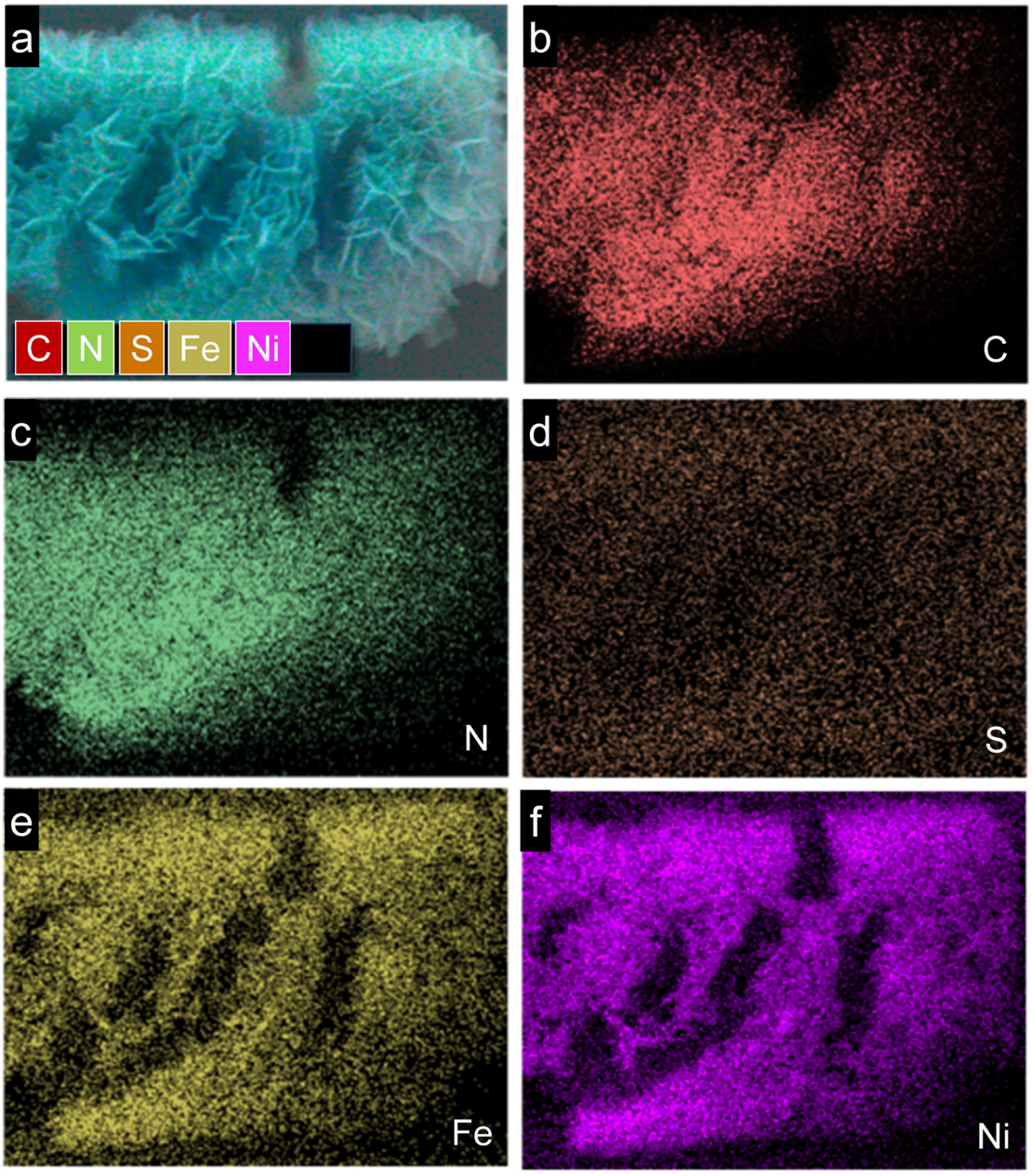

Fig. S1. EDS mapping for the SCN@NiFe.

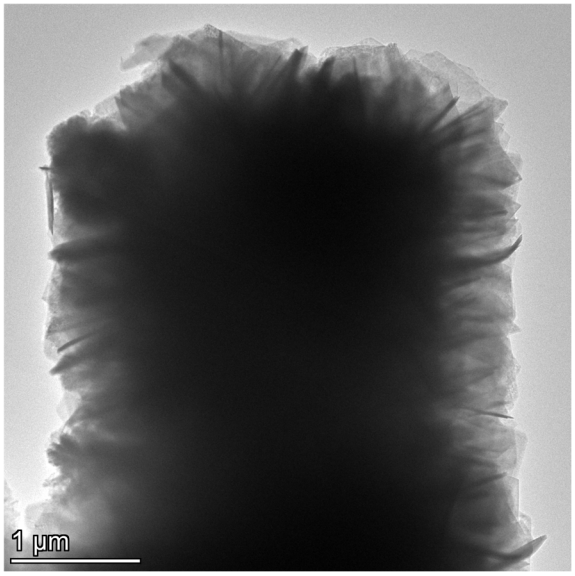

Fig. S2. TEM images of SCN@NiFe-32.

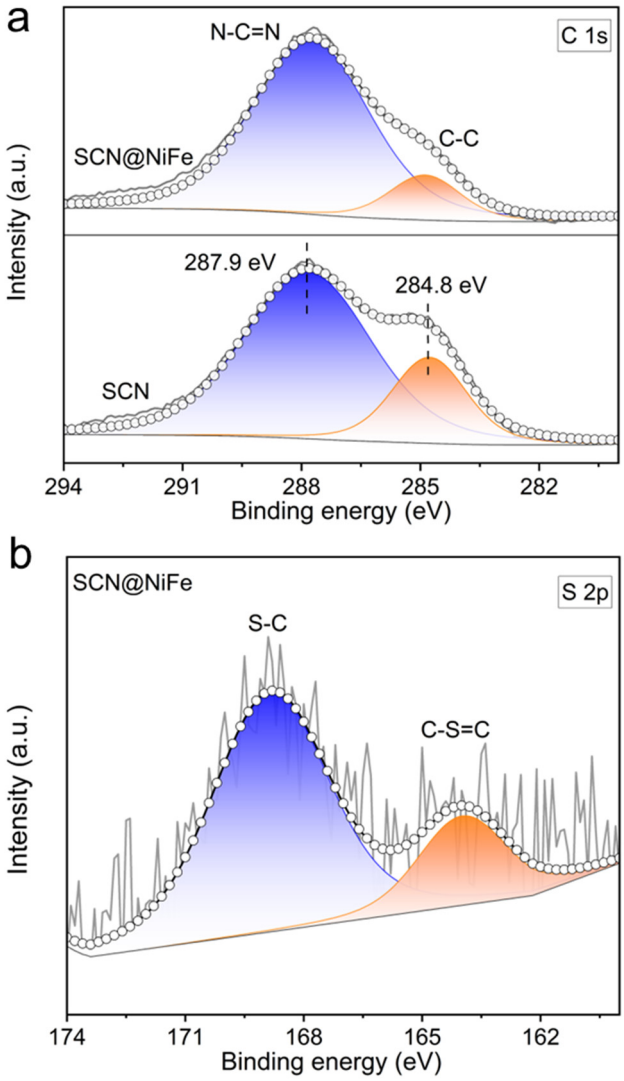

Fig. S3. High-resolution XPS spectra of (a) C 1s and (b) S 2p for SCN@NiFe and SCN.

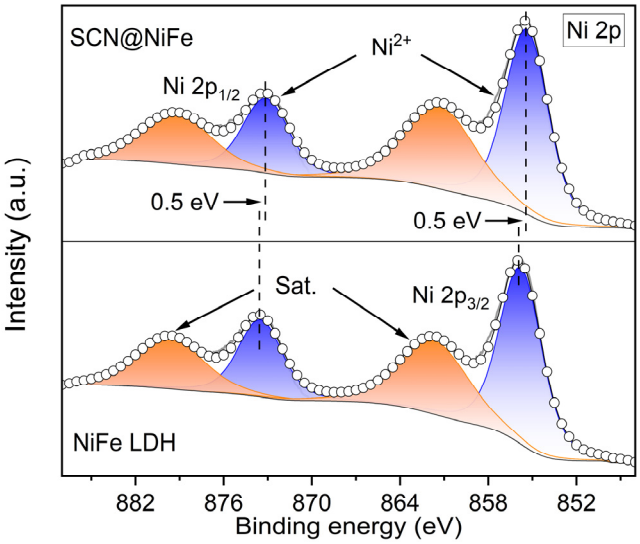

Fig. S4. High-resolution XPS spectra of Ni 2p for SCN@NiFe and NiFe LDH.

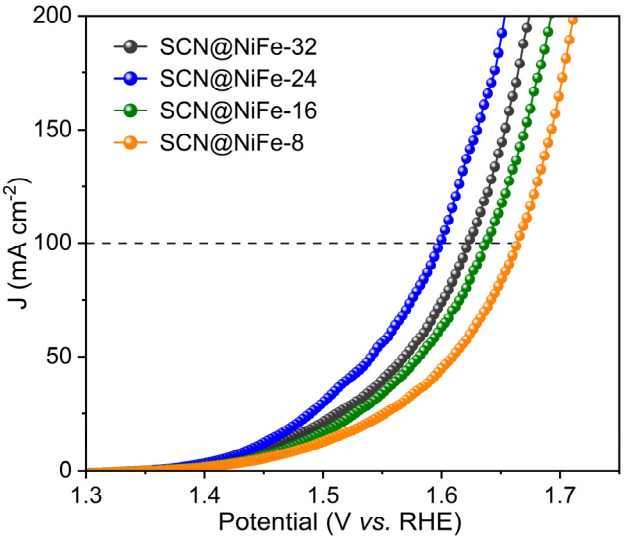

Fig. S5. OER performance of prepared SCN@NiFe-X (8, 16, 24, 32).

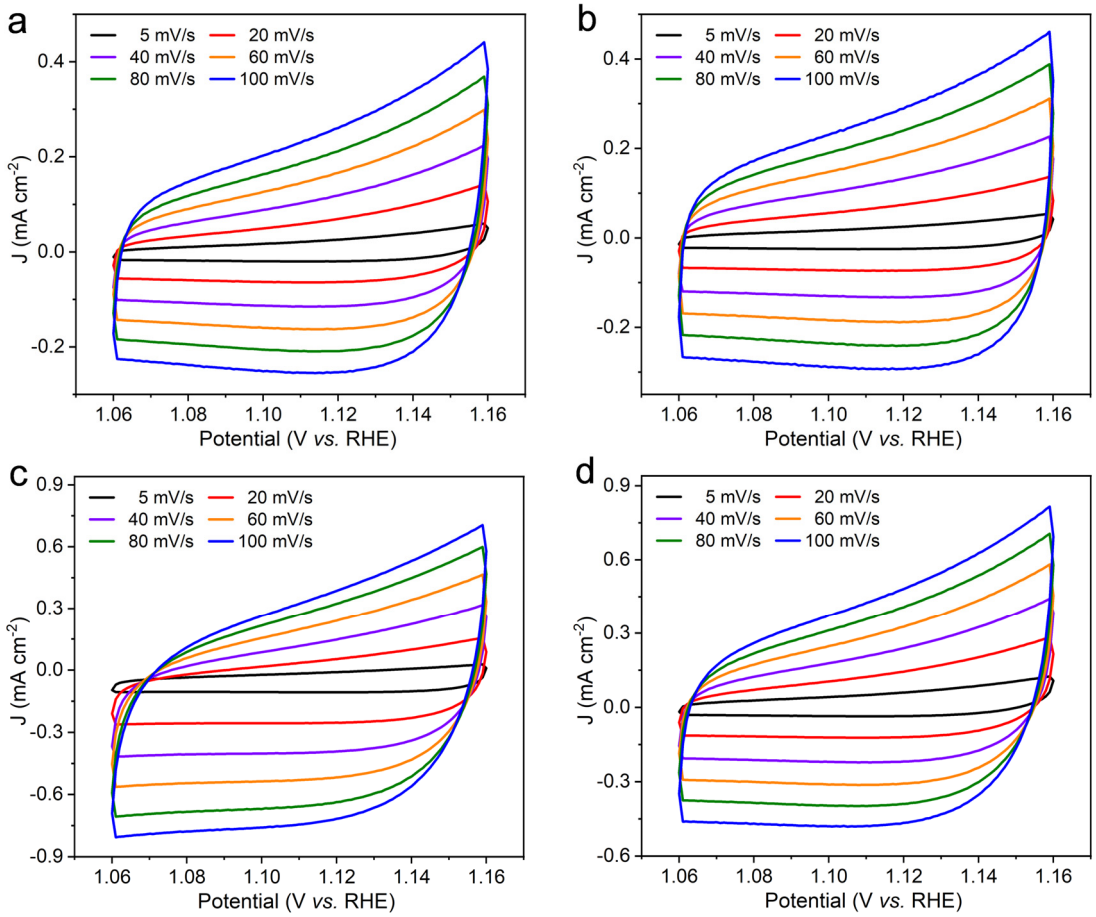

Fig. S6. CV curves at different scan rates. (a) SCN, (b) NiFe LDH, (c) SCN@NiFe, and (d) RuO_2 in the range from 1.06 V to 1.16 V vs. RHE for OER.

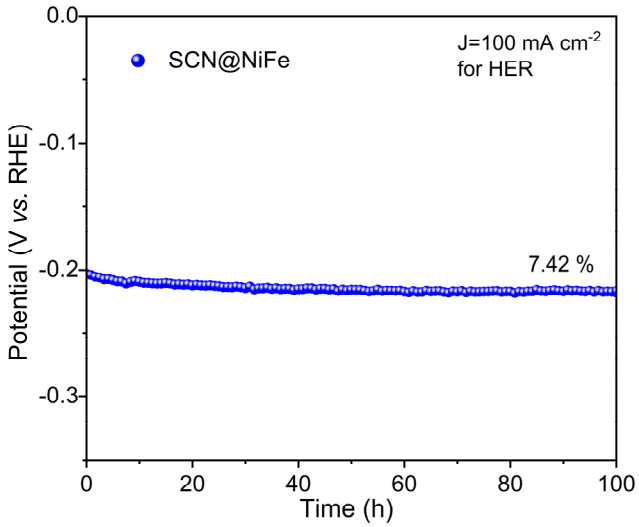

Fig. S7. Chronopotentiometry curve of SCN@NiFe during HER recorded at 100 mA cm^{-2} in 1 M KOH.

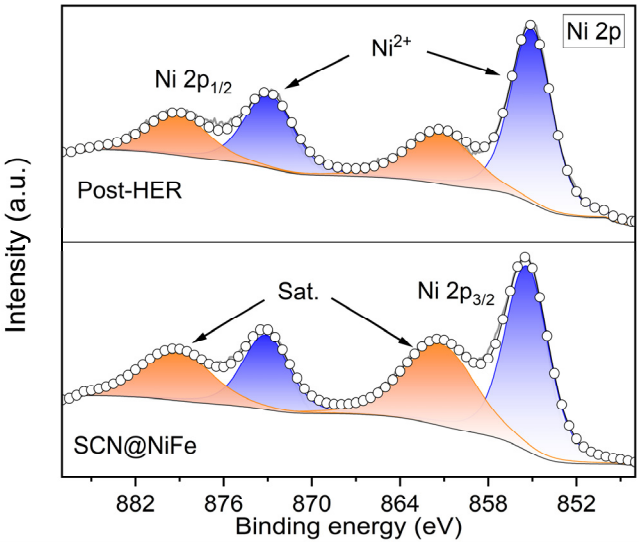

Fig. S8. XPS of Ni 2p for SCN@NiFe catalyst before and after the HER stability test in 1 M KOH.

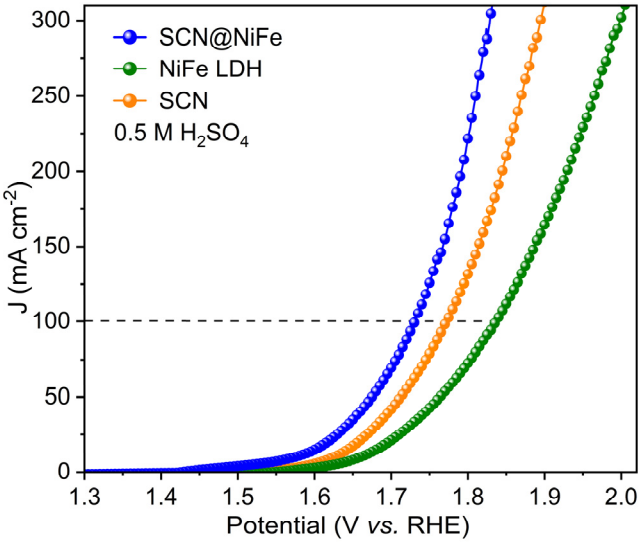

Fig. S9. Overall water splitting performance of prepared SCN, NiFe LDH, and SCN@NiFe in 0.5M H_2SO_4.

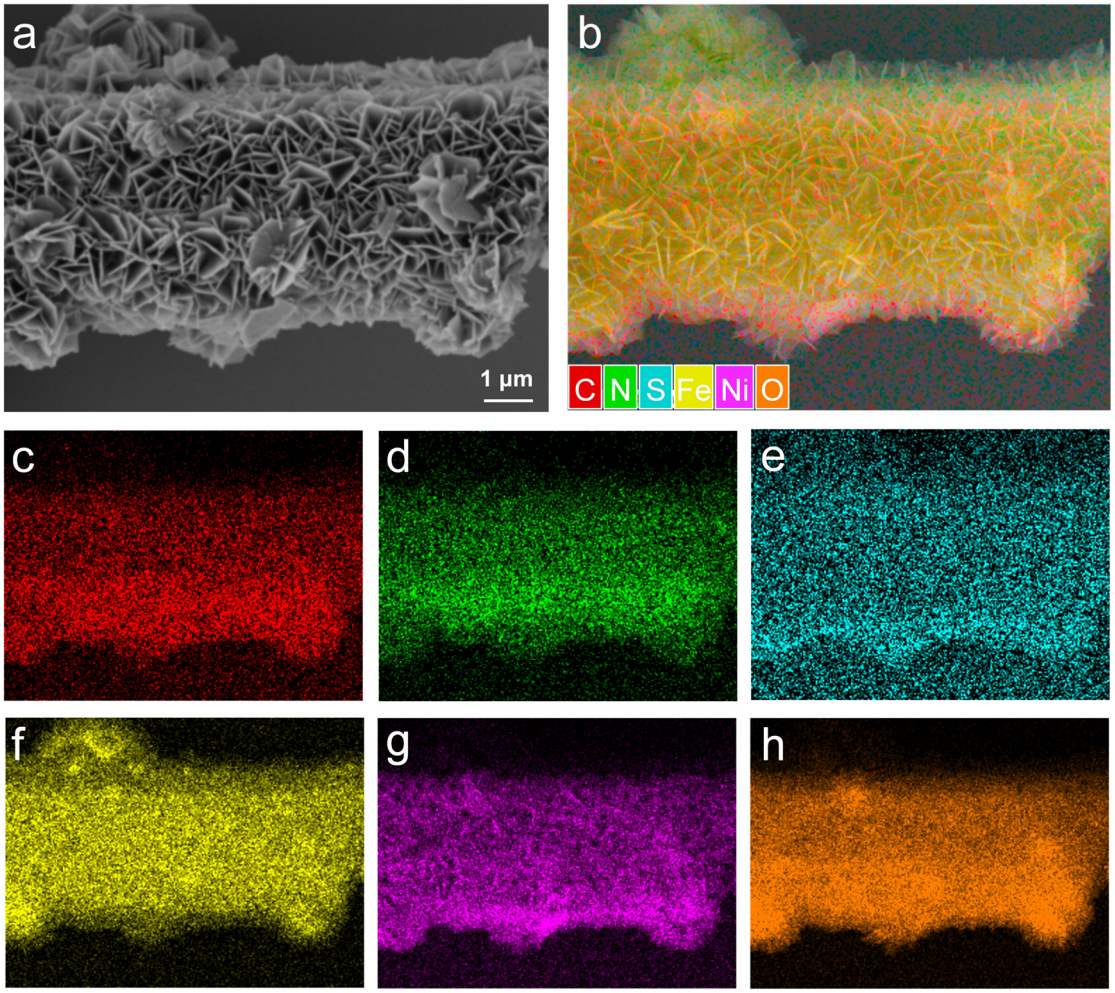

Fig. S10. (a) SEM image and (b-h) EDS mapping images of SCN@NiFe after the OER stability test in 0.5M H_2SO_4.

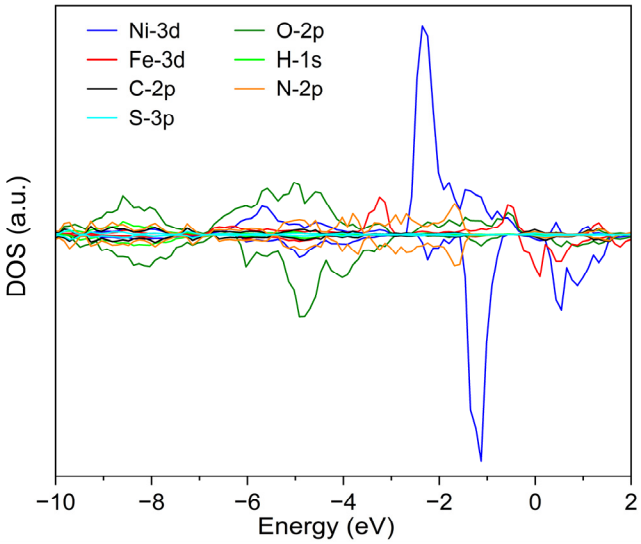

Fig. S11. The density of states of SCN@NiFe heterojunction.

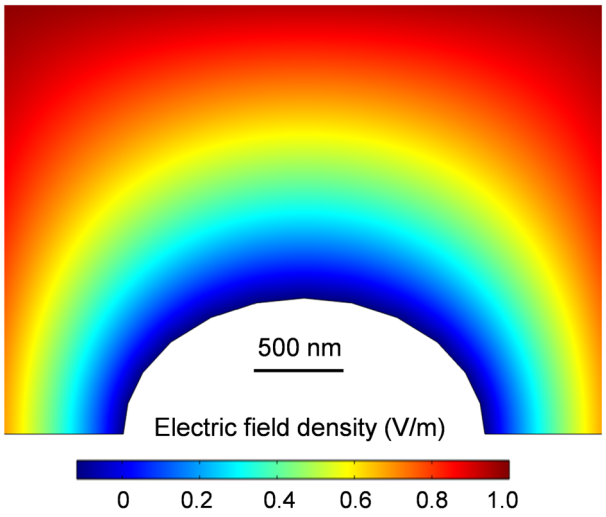

Fig. S12. Electric field distribution of SCN nanostructures.

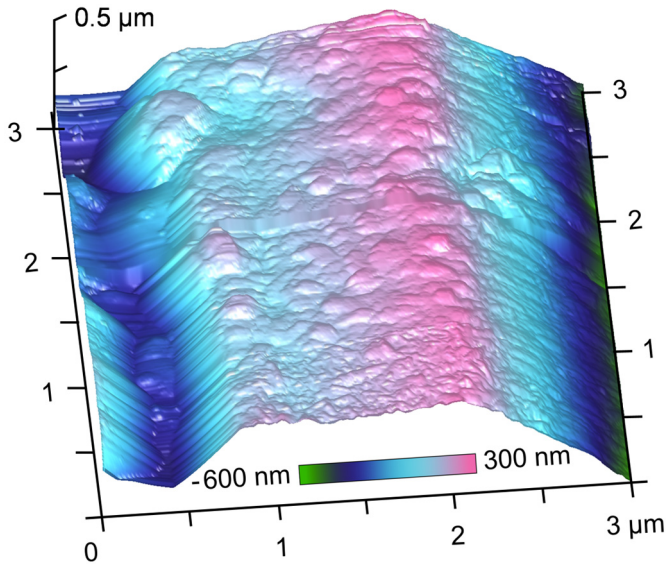

Fig. S13. 3D planar topographic images of the Kelvin probe force microscopy of the SCN@NiFe sample.

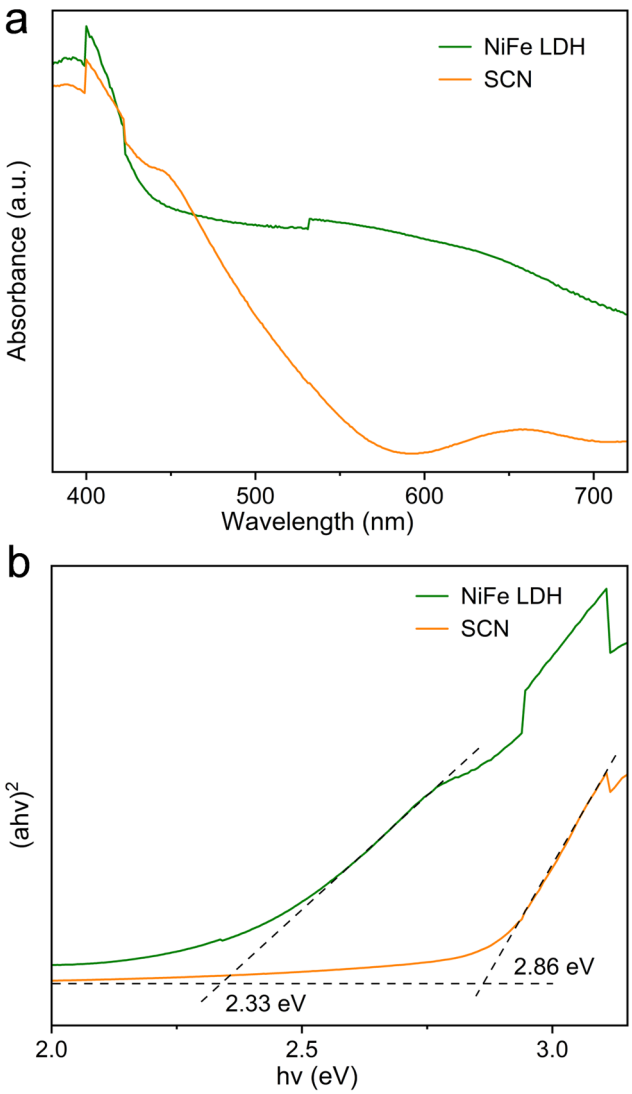

Fig. S14. (a) UV-vis absorbance spectra and (b) corresponding Tauc plots of SCN and NiFe LDH.

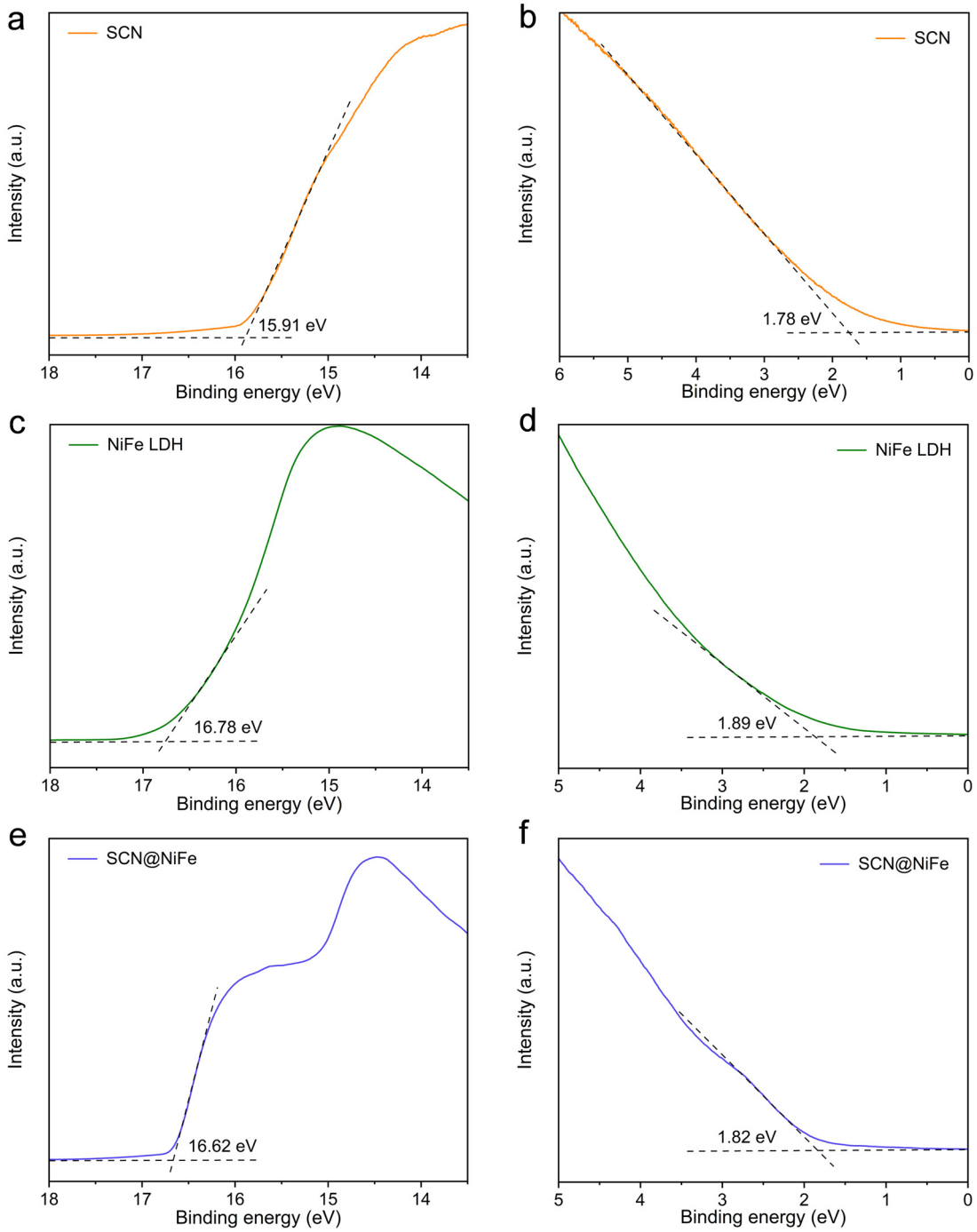

Fig. S15. UPS analysis of (a-b) SCN, (c-d) NiFe LDH, and (e-f) SCN@NiFe.

Table S1. The element contents of SCN@NiFe from XPS and SEM-EDS tests (at.%).

Means	C	N	O	S	Ni	Fe
XPS	28.35	23.69	26.05	0.81	8.41	12.69
SEM-EDS	29.30	23.65	25.13	0.84	8.79	12.38

Table S2. Comparison of the OER performance between SCN@NiFe and the recently reported heterojunction catalysts in 1 M KOH solution.

Electrocatalysts	Type	Current density ($mA\ cm^{-2}$)	η (mV)	Tafel slope ($mV\ dec^{-1}$)	Ref.
SCN@NiFe	**Schottky**	**10**	**233**	**41.5**	**This work**
CoP-CoO	p-p	10	210	90	[3]
NiMo@NiFeCe-LDH	Schottky	10	215	42.4	[4]
Ni/CeO_2@N-CNF	Schottky	10	230	54.2	[5]
Mo_2N-Co_xN	Schottky	10	247	105	[6]
V-Ni_3FeN/Ni@N-GTs	Schottky	10	252	46	[7]
$NiSe_2/FeSe_2$	p-p	10	256	50	[8]
$Se/NiSe_2$	Schottky	10	257	90	[9]
CeO_2/Co_3O_4	p-n	10	265	68.1	[10]
$Co_2P_2O_7$@N,P-C	Schottky	10	270	49.1	[11]
CoO/CeO_2	Schottky	10	297	75	[12]
$NiSe_2/CoSe_2$	p-p	10	304	69	[8]
Co/CoSe@NC	Schottky	10	335	52.6	[13]
$Co_2N_{0.67}$-BHPC	n-n	10	340	70	[14]
FeNi-LDH/CoP	p-n	20	231	33.5	[15]
$(Co(OH)_2)_4$@$La(OH)_3$	p-p	20	233	66.7	[16]
CuO@CoOOH	p-n	20	273	51.7	[17]
NiFe-LDH/Co_3O_4	p-n	50	274	81	[18]
Ni_2P/FeOOH	Schottky	100	246	62.8	[19]
MnCo-CH@NiFe-OH	p-n	100	250	49	[20]
$CoMn/CoMn_2O_4$	Schottky	100	380	68	[21]
CoFe-LDH@MXene	Schottky	200	330	82	[22]

Table S3. Comparison of SCN@NiFe and reported bifunctional electrocatalysts to obtain a cell voltage with a current density of 10 mA cm^{-2} in 1 M KOH solution.

Electrocatalysts	Cell voltage (V)	Ref.
SCN@NiFe	**1.51**	**This work**
Co/CoSe@NC	1.57	[13]
MnCo-CH@NiFe-OH	1.69	[20]
Ni/NiCoP	1.71	[23]
FeNi-LDH/CoP	1.73	[24]
$Ni/W_5N_4/NF$	1.77	[25]
$g\text{-}C_3N_4/rGO$	1.79	[26]
Fe_2P/CoP	1.79	[27]
$Co_8FeS_8@CoFe$	1.82	[28]
$Ni/MoO_2@CN$	1.83	[29]
$Ni_xB/Mo_{0.8}B_3$	1.85	[30]
CoP-CoO	1.86	[3]
Co/WC@NC	1.86	[31]
$B\text{-}C_3N_4@Fe_3C$	1.88	[32]
$MoS_2@Ni_{0.96}S$	1.88	[33]
$CoP/CoCr_2O_4$	1.89	[34]
$Se/NiSe_2$	1.91	[9]
$NiS_2/MoS_2/CNTs$	1.93	[35]
Ni-AC	1.94	[36]
$Co\text{-}Mo_2C\text{-}CN_x$	1.97	[37]

References

[1] G. Feng, F. Ning, J. Song, H. Shang, K. Zhang, Z. Ding, P. Gao, W. Chu, D. Xia, Sub-2 nm ultrasmall high-entropy alloy nanoparticles for extremely superior electrocatalytic hydrogen evolution, J. Am. Chem. Soc., 143 (2021) 17117-17127.

[2] H. Fei, J. Dong, M.J. Arellano-Jiménez, G. Ye, N. Dong Kim, E.L.G. Samuel, Z. Peng, Z. Zhu, F. Qin, J. Bao, M.J. Yacaman, P.M. Ajayan, D. Chen, J.M. Tour, Atomic cobalt on nitrogen-doped graphene for hydrogen generation, Nat. Commun., 6 (2015) 8668.

[3] J. Yao, M. Zhang, X. Ma, L. Xu, F. Gao, J. Xiao, H. Gao, Interfacial electronic modulation of CoP-CoO p-p type heterojunction for enhancing oxygen evolution reaction, J. Colloid Interface Sci., 607 (2022) 1343-1352.

[4] C. Yin, F. Zhou, J. Wu, X. Zhang, J. Wen, R. Zhu, M. Ma, S. Yoriya, P. He, Q. Fang, J. Wang, G. An, Strongly coupled NiMo@Alloy-LDH interfaces with low-barrier Schottky junctions for oxygen evolution reaction, Adv. Funct. Mater., 34 (2024) 2410429.

[5] T. Li, J. Yin, D. Sun, M. Zhang, H. Pang, L. Xu, Y. Zhang, J. Yang, Y. Tang, J. Xue, Manipulation of Mott-Schottky Ni/CeO_2 heterojunctions into N-doped carbon nanofibers for high-efficiency electrochemical water splitting, Small, 18 (2022) e2106592.

[6] H. Guo, A. Wu, Y. Xie, H. Yan, D. Wang, L. Wang, C. Tian, 2D porous molybdenum nitride/cobalt nitride heterojunction nanosheets with interfacial electron redistribution for effective electrocatalytic overall water splitting, J. Mater. Chem. A, 9 (2021) 8620-8629.

[7] G. Song, S. Luo, Q. Zhou, J. Zou, Y. Lin, L. Wang, G. Li, A. Meng, Z. Li, Doping and heterojunction strategies for constructing V-doped Ni_3FeN/Ni anchored on N-doped graphene tubes as an efficient overall water splitting electrocatalyst, J. Mater. Chem. A, 10 (2022) 18877-18888.

[8] S. Ni, H. Qu, Z. Xu, X. Zhu, H. Xing, L. Wang, J. Yu, H. Liu, C. Chen, L. Yang, Interfacial engineering of the $NiSe_2$/$FeSe_2$ p-p heterojunction for promoting oxygen evolution reaction and electrocatalytic urea oxidation, Appl. Catal. B: Environ., 299 (2021) 120638.

[9] S. Khatun, P. Roy, Mott-Schottky heterojunction of Se/$NiSe_2$ as bifunctional electrocatalyst for energy efficient hydrogen production via urea assisted seawater electrolysis, J. Colloid Interface Sci., 630 (2023) 844-854.

[10] B. Qiu, C. Wang, N. Zhang, L. Cai, Y. Xiong, Y. Chai, CeO_2-induced interfacial Co^{2+} octahedral sites and oxygen vacancies for water oxidation, ACS Catal., 9 (2023) 6484-6490.

[11] D. Liang, C. Lian, Q. Xu, M. Liu, H. Liu, H. Jiang, C. Li, Interfacial charge polarization in $Co_2P_2O_7$@N, P co-doped carbon nanocages as Mott-Schottky electrocatalysts for accelerating oxygen evolution reaction, Appl. Catal. B: Environ., 268 (2020) 118417.

[12] L. Zhang, Y. Lei, Y. Yang, D. Wang, Y. Zhao, X. Xiang, H. Shang, B. Zhang, High coverage sub-nano iridium cluster on core-shell cobalt-cerium bimetallic oxide for highly efficient sull-pH water splitting, Adv. Sci., 11 (2024) 2407475.

[13] K. Li, R. Cheng, Q. Xue, P. Meng, T. Zhao, M. Jiang, M. Guo, H. Li, C. Fu, In-situ construction of Co/CoSe Schottky heterojunction with interfacial electron redistribution to facilitate oxygen electrocatalysis bifunctionality for zinc-air batteries, Chem. Eng. J., 450 (2022) 137991.

[14] X. Lv, Z. Xiao, H. Wang, X. Wang, L. Shan, F. Wang, C. Wei, X. Tang, Y. Chen, In situ construction of Co/N/C-based heterojunction on biomass-derived hierarchical porous carbon with stable active sites using a Co-N protective strategy for high-efficiency ORR, OER and HER trifunctional electrocatalysts, J. Energ. Chem., 54 (2021) 626-638.

[15] K. He, T. Tadesse, X. Liu, J. Zai, X. Li, X. Liu, W. Li, N. Ali, X. Qian, Utilizing the space-charge region of the FeNi-LDH/CoP p-n junction to promote performance in oxygen evolution electrocatalysis, Angew. Chem. Int. Ed., 58 (2019) 11903-11909.
[16] L. Gao, Y. Li, G. Li, J. Huo, L. Jia, Interface charge induced self-assembled $(Co(OH)_2)_4$@$La(OH)_3$ heterojunction derived from Co_4-MOF@$La(HCO_2)_3$ to boost oxygen evolution reaction, Chem. Eng. J., 451 (2023) 138743.
[17] J. Hu, A. Al-Salihy, J. Wang, X. Li, Y. Fu, Z. Li, X. Han, B. Song, P. Xu, Improved interface charge transfer and redistribution in CuO-CoOOH p-n heterojunction nanoarray electrocatalyst for enhanced oxygen evolution reaction, Adv. Sci., 8 (2021) 2103314.
[18] Y. Zhang, P. Guo, S. Niu, J. Wu, W. Wang, B. Song, X. Wang, Z. Jiang, P. Xu, Magnetic field enhanced electrocatalytic oxygen evolution of NiFe-LDH/Co_3O_4 p-n heterojunction supported on nickel foam, Small Methods, 6 (2022) e2200084.
[19] Y. Zhang, L. You, Q. Liu, Y. Li, T. Li, Z. Xue, G. Li, Interfacial charge transfer in a hierarchical Ni_2P/FeOOH heterojunction facilitates electrocatalytic oxygen evolution, ACS Appl. Mater. Interfaces, 13 (2021) 2765-2771.
[20] Y. Zeng, Z. Cao, J. Liao, H. Liang, B. Wei, X. Xu, H. Xu, J. Zheng, W. Zhu, L. Cavallo, Z. Wang, Construction of hydroxide pn junction for water splitting electrocatalysis, Appl. Catal. B: Environ., 292 (2021) 120160.
[21] C. Wang, H. Lu, Z. Mao, C. Yan, G. Shen, X. Wang, Bimetal schottky heterojunction boosting energy-saving hydrogen production from alkaline water via urea electrocatalysis, Adv. Funct. Mater., 30 (2020) 2000556.
[22] L. Deng, K. Zhang, D. Shi, S. Liu, D. Xu, Y. Shao, J. Shen, Y. Wu, X. Hao, Rational design of Schottky heterojunction with modulating surface electron density for high-performance overall water splitting, Appl. Catal. B: Environ., 299 (2021) 120660.
[23] Y. Lin, Y. Pan, S. Liu, K. Sun, Y. Cheng, M. Liu, Z. Wang, X. Li, J. Zhang, Construction of multi-dimensional core/shell Ni/NiCoP nano-heterojunction for efficient electrocatalytic water splitting, Appl. Catal. B: Environ., 259 (2019) 118039.
[24] K. He, T. Tadesse Tsega, X. Liu, J. Zai, X.-H. Li, X. Liu, W. Li, N. Ali, X. Qian, Utilizing the space-charge region of the FeNi-LDH/CoP p-n junction to promote performance in oxygen evolution electrocatalysis, Angew. Chem. Int. Ed., 58 (2019) 11903-11909.
[25] Y. Zhou, B. Chu, Z. Sun, L. Dong, F. Wang, B. Li, M. Fan, Z. Chen, Surface reconstruction and charge distribution enabling Ni/W_5N_4 Mott-Schottky heterojunction bifunctional electrocatalyst for efficient urea-assisted water electrolysis at a large current density, Appl. Catal. B: Environ., 323 (2023) 122168.
[26] H. Choi, S. Surendran, Y. Sim, M. Je, G. Janani, H. Choi, J.K. Kim, U. Sim, Enhanced electrocatalytic full water-splitting reaction by interfacial electric field in 2D/2D heterojunction, Chem. Eng. J., 450 (2022) 137789.
[27] X. Ding, J. Yu, W. Huang, D. Chen, W. Lin, Z. Xie, Modulation of the interfacial charge density on Fe_2P – CoP by coupling CeO_2 for accelerating alkaline electrocatalytic hydrogen evolution reaction and overall water splitting, Chem. Eng. J., 451 (2023) 138550.
[28] T. Zhao, D. Zhong, L. Tian, G. Hao, G. Liu, J. Li, Q. Zhao, Constructing abundant phase interfaces of the sulfides/metal-organic frameworks p-p heterojunction array for efficient overall water splitting and urea electrolysis, J. Colloid Interface Sci., 634 (2023) 630-641.
[29] T. Zhou, Y. Qi Huang, A. Ali, P. Kang Shen, Ni-MoO_2 nanoparticles heterojunction loaded on

stereotaxically-constructed graphene for high-efficiency overall water splitting, J. Electroanal. Chem., 897 (2021) 115555.
[30] M. Rafiq, K. Harrath, M. Feng, R. Li, A.R. Woldu, P.K. Chu, L. Hu, F. Lu, X. Yao, NixB/$Mo_{0.8}B_3$ nanorods encapsulated by a boron-rich amorphous layer for universal pH water splitting at the ampere level, Adv. Energy Mater., 14 (2024) 2402866.
[31] G. Raj, D. Das, B. Sarkar, S. Biswas, K.K. Nanda, Universal avenue to metal-transition metal carbide grafted N-doped carbon framework as efficient dual Mott-Schottky electrocatalysts for water splitting, Sustainable Mater. Technol., 33 (2022) e00451.
[32] G. Yang, T. Yang, Z. Wang, K. Wang, M. Zhang, P.D. Lund, S. Yun, Targeted doping induces interfacial orientation for constructing surface-functionalized Schottky junctions to coordinate redox reactions in water electrolysis, Adv. Powder Mater., 3 (2024) 100224.
[33] S. Liu, B. Li, S.V. Mohite, P. Devaraji, L. Mao, R. Xing, Ultrathin MoS_2 nanosheets in situ grown on rich defective $Ni_{0.96}S$ as heterojunction bifunctional electrocatalysts for alkaline water electrolysis, Int. J. Hydrog. Energy, 45 (2020) 29929-29937.
[34] A. Saad, H. Shen, Z. Cheng, Q. Ju, H. Guo, M. Munir, A. Turak, J. Wang, M. Yang, Three-dimensional mesoporous phosphide-spinel oxide heterojunctions with dual function as catalysts for overall water splitting, ACS Appl. Energy Mater., 3 (2020) 1684-1693.
[35] G.-L. Li, Y.-Y. Miao, X.-Y. Qiao, T.-Y. Wang, F. Deng, Engineering edge sites based on NiS_2/MoS_2/CNTs heterojunction catalyst for overall water splitting, Appl. Surf. Sci., 615 (2023) 156309.
[36] H. Zhang, J.-W. Zhang, T.-Z. Ren, Z.-Y. Yuan, T.J. Bandosz, Ni-doped hierarchical porous carbon with a p/n-junction promotes electrochemical water splitting, Int. J. Hydrog. Energy, 45 (2020) 17493-17503.
[37] P. Zhang, Y. Liu, T. Liang, E.H. Ang, X. Zhang, F. Ma, Z. Dai, Nitrogen-doped carbon wrapped Co-Mo_2C dual Mott-Schottky nanosheets with large porosity for efficient water electrolysis, Appl. Catal. B: Environ., 284 (2021) 119738.